Rashba and Dresselhaus Effects in Hybrid Organic–Inorganic Perovskites: From Basics to Devices

Mikaël Kepenekian,*,† Roberto Robles,‡ Claudine Katan,† Daniel Sapori,§ Laurent Pedesseau,§ and Jacky Even*,§

†Institut des Sciences Chimiques de Rennes, UMR 6226, CNRS - Université de Rennes 1 35700 Rennes, France, ‡ICN2 - Institut Catala de Nanociencia i Nanotecnologia, Campus UAB, 08193 Bellaterra, Barcelona, Spain, and §Université Européenne de Bretagne, INSA, FOTON UMR 6082, 35708 Rennes, France

ABSTRACT We use symmetry analysis, density functional theory calculations, and $k \cdot p$ modeling to scrutinize Rashba and Dresselhaus effects in hybrid organic–inorganic halide perovskites. These perovskites are at the center of a recent revolution in the field of photovoltaics but have also demonstrated potential for optoelectronic applications such as transistors and light emitters. Due to a large spin–orbit coupling of the most frequently used metals, they are also predicted to offer a promising avenue for spin-based applications. With an in-depth inspection of the electronic structures and bulk lattice symmetries of a variety of systems, we analyze the origin of the spin splitting in two- and three-dimensional hybrid perovskites. It is shown that low-dimensional nanostructures made of $CH_3NH_3PbX_3$ (X = I, Br) lead to spin splittings that can be controlled by an applied electric field. These findings further open the door for a perovskite-based spintronics.

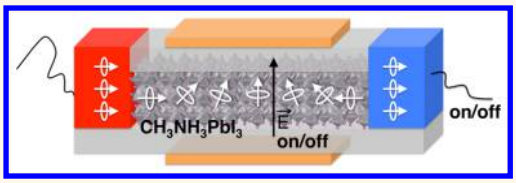

KEYWORDS: perovskite · DFT · spin–orbit · Rashba · spin-FET · ferroelectric · nanostructure

Since 2009 and the pioneer work of Miyasaka and co-workers,[1] three-dimensional (3D) solution-processed hybrid organic–inorganic halide perovskites AMX_3 (where A is an organic cation, M = Pb, Sn, or Ge, and X = I, Br, or Cl) have attracted increasing attention from the photovoltaic community. Such a craze arises from the early successes met in improving the efficiency in the solar-to-electricity conversion, from 3.8%[1] up to 20.1%[2] in only five years, combined with low costs of production.[3–5] Prior to the solar cell intense activity, hybrid halide perovskites were most popular in their two-dimensional (2D), that is, layered, form because they have shown good potential for applications in optoelectronics and microelectronics.[6–8] The wide range of applications of these materials results from the impressive diversity of structures that can be obtained by varying their composition.

Although perovskites have been studied for decades, it is only recently that the major role of spin–orbit coupling (SOC) has been underlined by calculations based on density functional theory (DFT).[9–11] Besides an improved description of their band structures and optoelectronic properties, it has led to the prediction of Rashba or Dresselhaus spin splitting or both in these hybrid systems. Dresselhaus[12] and Rashba[13] effects originally corresponded to spin splittings in zinc-blende and würtzite structures, respectively. Later, Bychkov and Rashba pointed out that the Rashba term also occurs in quasi-2D systems.[14] These effects have been extensively studied[15–19] and have been observed in various systems such as heterostructures,[20,21] quantum wells (QWs),[22–25] bulks,[26–28] heavy atoms and alloy surfaces,[16,27,29–36] or nanowires (NWs).[37–39] The control of spin-dependent band structure provides the opportunity to manipulate the spin with potential applications in spintronics.[40–43] Rashba and Dresselhaus effects have also raised interest in the realization of topological superconductors for topological quantum information processing through the generation of Majorana fermions.[44,45] In the case of hybrid halide perovskites, a Rashba spin splitting has been predicted in methylammonium-based perovskites $CH_3NH_3MX_3$,[11,46–48] and in formamidinium tin iodide $CH(NH_2)_2SnI_3$.[49] Hybrid halide perovskite-based spintronics

* Address correspondence to mikael.kepenekian@univ-rennes1.fr, jacky.even@insa-rennes.fr.

Received for review July 16, 2015 and accepted September 8, 2015.

Published online 10.1021/acsnano.5b04409

is also supported by recent experimental studies on ferroelectric domains in thin films[50] and on the spin dynamics in $CH_3NH_3PbI_3$ that determined a spin relaxation lifetime around 7 ps.[51]

In this work, we conduct a survey on two- and three-dimensional hybrid halide perovskites. On the basis of symmetry analysis and DFT calculations, we discuss the possibility of designing spintronic devices based on these materials. We start by recalling general features of Rashba and Dresselhaus spin splittings. We focus then on systems presenting a non-centrosymmetric space group, which naturally exhibit a Rashba or Dresselhaus splitting. Finally, we show that a centrosymmetric system can present a tunable splitting through external electric field. The latter result opens the way for perovskite-based spintronics applications.

RESULTS AND DISCUSSION

Spin−Orbit Coupling and Symmetry Point Groups: Rashba and Dresselhaus Spin Splittings. In the presence of SOC, we consider the following Hamiltonian

$$\mathscr{H} = \frac{\mathbf{p}^2}{2m} + V + \mathscr{H}_{SO}$$

where V is the lattice periodic crystal potential and $\mathscr{H}_{SO}$ is the spin−orbit interaction term,

$$\mathscr{H}_{SO} = \frac{\hbar}{4m^2c^2}(\nabla V \times \mathbf{p})\cdot\sigma$$

where $\hbar$ is Planck's constant, m is the mass of an electron, c is the velocity of light, $\mathbf{p}$ is the momentum operator, and $\boldsymbol{\sigma} = (\sigma_x, \sigma_y, \sigma_z)$ is the vector of Pauli spin matrices. Starting from a Bloch states description,

$$\psi_{n\mathbf{k}}(\mathbf{r}) = e^{i\mathbf{k}\cdot\mathbf{r}}\,\phi_{n\mathbf{k}}(\mathbf{r})$$

the eigenvalue problem for $\phi_{n\mathbf{k}}$ reads

$$(\mathscr{H}^0(\mathbf{k}) + \mathscr{H}_{SO}(\mathbf{k}))\phi_{n\mathbf{k}}(\mathbf{r}) = \varepsilon_n(\mathbf{k})\phi_{n\mathbf{k}}(\mathbf{r})$$

with

$$\mathscr{H}^0(\mathbf{k}) = \frac{(\hbar\mathbf{k} + \mathbf{p}^2)}{2m} + V$$

$$\mathscr{H}_{SO}(\mathbf{k}) = \frac{\hbar}{4m^2c^2}(\nabla V \times (\hbar\mathbf{k} + \mathbf{p})\cdot\sigma)$$

It is common to treat SOC as a perturbation of the $\mathscr{H}^0$ zero-order Hamiltonian, which is solved following the $\mathbf{k}\cdot\mathbf{p}$ expansion around a given $\mathbf{k}_0$ leading to $\phi^0_{n\mathbf{k}}$, which is the solution of the unperturbed Hamiltonian with eigenvalue $\varepsilon^0_n(\mathbf{k})$. It is completed by a spin function χ_s ($s = \pm 1/2$), keeping $\phi^0_{n\mathbf{k}s} = \phi^0_{n\mathbf{k}}\chi_s$ an eigenvector of $\mathscr{H}^0(\mathbf{k})$. We will denote $\phi^0_{n\mathbf{k}\uparrow}$, $\phi^0_{n\mathbf{k}\downarrow}$ the spinors and $\epsilon^0_{n\uparrow}(\mathbf{k})$, $\epsilon^0_{n\downarrow}(\mathbf{k})$ the corresponding eigenvalues for $s = +1/2$ and $-1/2$, respectively.

The time reversal symmetry is conserved by SOC and delivers general conditions for conjugated spinors (Kramers' degeneracy)

$$\varepsilon^0_{n\uparrow}(\mathbf{k}) = \varepsilon^0_{n\downarrow}(-\mathbf{k}) \quad \text{and} \quad \varepsilon^0_{n\downarrow}(\mathbf{k}) = \varepsilon^0_{n\uparrow}(-\mathbf{k})$$

Inversion symmetry yields additional conditions

$$\varepsilon^0_{n\uparrow}(\mathbf{k}) = \varepsilon^0_{n\uparrow}(-\mathbf{k}) \quad \text{and} \quad \varepsilon^0_{n\downarrow}(\mathbf{k}) = \epsilon^0_{n\downarrow}(-\mathbf{k})$$

Combining both symmetries leads to a double spin degeneracy

$$\varepsilon^0_{n\uparrow}(\mathbf{k}) = \varepsilon^0_{n\downarrow}(\mathbf{k})$$

across all the dispersion diagram within the Brillouin zone (BZ). When inversion symmetry is lost, the later spin degeneracy condition can be lost for a general wave vector, except for special high symmetry points leading to a band splitting.[11,52]

We consider $\mathbf{k}_0$, a special symmetry point of the BZ for which the spin degeneracy is conserved. The in-plane wave vector $\mathbf{k}_\parallel$ is naturally defined for a 2D electron gas. In a 3D system, it belongs to the plane normal to a high symmetry axis defining $\mathbf{k}_\perp$. Then one can apply the quasi-degenerate perturbation theory with the perturbative Hamiltonian, that is, the Rashba Hamiltonian,[15]

$$\mathscr{H}_R = \alpha(\mathbf{k})\cdot\sigma \qquad (1)$$

with

$$\alpha(\mathbf{k}) = \langle\phi_{n\mathbf{k}}|\frac{\hbar}{4m^2c^2}(\nabla V \times (\hbar\mathbf{k} + \mathbf{p}))|\phi_{n\mathbf{k}}\rangle$$

Taking advantage of the symmetry allows us to sort terms and identify the vanishing ones. The polynomial form of α has been previously derived in different works.[15,17,53] Clearly, due to time reversal symmetry, only odd power terms are relevant in the development. Vajna and co-workers[53] have precisely described how to determine the linear and cubic terms of $\mathscr{H}_R$ thanks to irreducible representations of relevant point groups for C_n and C_{nv} ($n = 2, 3, 4$). It has been recently completed for the D_{2d} point groups.[17]

Let us illustrate these results with the example of a quasi-2D system in C_{2v} symmetry. Limiting the expansion to linear terms, only four contributions have to be considered: $k_x\sigma_y$, $k_y\sigma_x$, $k_x\sigma_x$, and $k_y\sigma_y$. It leads to the Rashba−Dresselhaus Hamiltonian:

$$H_{RD}(\mathbf{k}_\parallel) = \lambda_R(k_x\sigma_y - k_y\sigma_x) + \lambda_D(k_x\sigma_x - k_y\sigma_y) \qquad (2)$$

where $\mathbf{k}_\parallel = (\mathbf{k}_x, \mathbf{k}_y)$ and $\mathbf{k}_\perp = \mathbf{k}_z$. For $\lambda_D = 0$, we retrieve the pure Rashba effect (also known as Bychkov−Rashba effect) that traces back to site inversion asymmetry (SIA) found in conventional semiconductor quantum structures.[15] For $\lambda_R = 0$, the remaining term is commonly found in zinc blende structures and related to the so-called bulk inversion asymmetry (BIA).[15] It is labeled here as the Dresselhaus effect. The solution of the eigenvalue problem gives us the dispersion relations for the upper (E_{RD+}) and lower (E_{RD-})

branches away from $\mathbf{k_0}$, as well as the corresponding eigenvectors:

$$E_{RD\pm}(\mathbf{k}_{||}) = \frac{\hbar k_{||}^2}{2m} \pm \sqrt{(\lambda_D^2 + \lambda_R^2)(k_x^2 + k_y^2) - 4\lambda_D\lambda_R k_x k_y} \quad (3)$$

$$\Psi_{RD\pm}(\mathbf{k}_{||}) = \frac{e^{i\mathbf{k}_{||}\cdot\mathbf{r}}}{2\pi\hbar}\frac{1}{\sqrt{2}}\begin{pmatrix} \mp\dfrac{-\lambda_D(k_x + ik_y) + i\lambda_R(k_x - ik_y)}{\sqrt{(\lambda_D^2 + \lambda_R^2)(k_x^2 + k_y^2) - 4\lambda_D\lambda_R k_x k_y}} \\ 1 \end{pmatrix} \quad (4)$$

If $\lambda_D = 0$, then the energy splitting $\Delta E_R = E_{R+} - E_{R-}$ is given by

$$\Delta E_R(\mathbf{k}_{||}) = 2\lambda_R\sqrt{k_x^2 + k_y^2} \quad (5)$$

The same relation exists with λ_D if λ_R vanishes. Then, in both limiting cases, the nonzero coefficient λ is related to the band splitting away from the high symmetry point and reads

$$\lambda = \frac{\Delta E(\mathbf{k}_{||})}{2\sqrt{k_x^2 + k_y^2}} \quad (6)$$

with $\Delta E = E_+ - E_-$ (Figure 1a). In mixed cases, the band splitting alone cannot discriminate the relative strength of Rashba and Dresselhaus effects and the expectation value of the Pauli operator $\langle\boldsymbol{\sigma}\rangle_{RD\pm} = \langle\Psi_{RD\pm}|\boldsymbol{\sigma}|\Psi_{RD\pm}\rangle$ must also be considered.

It is convenient to write $\mathbf{k}_{||} = k_{||}(\cos\theta, \sin\theta, 0)$, then the eigenvectors of H_{RD} are given by

$$\Psi_{RD\pm} = \frac{e^{i\mathbf{k}_{||}\cdot\mathbf{r}}}{2\pi\hbar}\frac{1}{\sqrt{2}}\begin{pmatrix} \mp\dfrac{-\lambda_D e^{i\theta} + i\lambda_R e^{-i\theta}}{\sqrt{\lambda_D^2 + \lambda_R^2 - 2\lambda_D\lambda_R \sin 2\theta}} \\ 1 \end{pmatrix} \quad (7)$$

In the pure Rashba case ($\lambda_D = 0$), the expectation value becomes

$$\langle\sigma\rangle_{R\pm} \propto \pm\begin{pmatrix} -\sin\theta \\ \cos\theta \\ 0 \end{pmatrix} \quad (8)$$

We recover the well-known Rashba feature (Figure 1b) with an in-plane orientation always orthogonal to the momentum direction. On the other hand, in the case of a pure Dresselhaus effect ($\lambda_R = 0$), one obtains

$$\langle\sigma\rangle_{D\pm} \propto \pm\begin{pmatrix} \cos\theta \\ -\sin\theta \\ 0 \end{pmatrix} \quad (9)$$

which leads to very different spin textures (Figure 1c) for the inner and outer branches, characteristic of a BIA spin splitting. The general case reads

$$\langle\sigma\rangle_{RD\pm} \propto \pm\begin{pmatrix} \lambda_D\cos\theta - \lambda_R\sin\theta \\ -\lambda_D\sin\theta + \lambda_R\cos\theta \\ 0 \end{pmatrix} \quad (10)$$

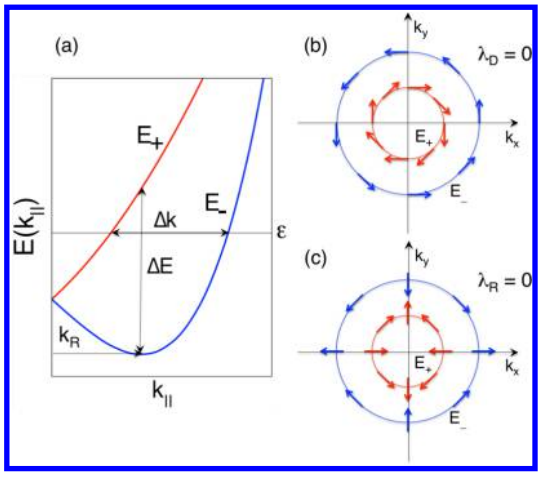

Figure 1. (a) Dispersion for the inner (E_+, red line) and outer (E_-, blue line) branches for a system in C_{2v} symmetry ruled by the Rashba–Dresselhaus Hamiltonian. The minimum momentum displacement is denoted k_R and the amplitude of the energy ΔE and momentum Δk splittings are also shown. (b) Scheme of spin orientations for the corresponding eigenstates $\Psi_{RD\pm}$ in the case of pure Rashba effect (or SIA), that is, $\lambda_D = 0$. (c) Same in the case of pure Dresselhaus Hamiltonian (or BIA), that is, $\lambda_R = 0$.

Thus, once $\langle\boldsymbol{\sigma}\rangle_\pm$ is computed, one can deduce the relative strength of each effect. In the case of C_{2v} symmetry, the spin distribution remains in-plane, even going to cubic terms. The situation is different with C_{3v} and D_{2d} point groups where the Hamiltonian can contain cubic terms depending on σ_z. In that case, nonzero out-of-plane components of the spinors can occur.

The computational observation of the spin splittings is performed by computing the band structure around a high-symmetry point of the BZ. One has to be careful to properly define $\mathbf{k}_{||}$ based on the symmetry of the system. In addition, the spin texture is computed as well to identify and assess the existence and relative amplitudes of Rashba and Dresselhaus effects. In the following, we conduct a survey on various hybrid organic–inorganic perovskites structures.

Rashba-type splittings have been designed and observed among QWs[22−25] and heterostructures[20,21] of conventional semiconductors.[15] Hybrid organic–inorganic perovskites appear to be promising candidates in that respect since they present giant SOC.[9,10] Moreover, this family of compounds can be found in many different crystal structures. To conduct our survey, we decided to start from the highly symmetrical $Pm\bar{3}m$ (no. 221) reference phase,[52] observed in the high temperature phase of numerous hybrid perovskites.[54−57] From this point, we follow different phase transitions (Figure 2). A key point in the observation of a SOC induced spin splitting is the loss of inversion symmetry. Therefore, we take interest in non-centrosymmetric structures, such as ferroelectric structures. We consider 3D bulk examples belonging to *P4mm* (no. 99), *R3m* (no. 160), and *Amm2* (no. 38) crystal groups. Then, we consider the case of a temperature induced ferroelectric

transition in a bulk 2D perovskite. Finally, we investigate the effect of an external electric field starting with a structure having inversion symmetry that should not be suitable candidates for Rashba or Dresselhaus effect. With the example of $CH_3NH_3PbX_3$ we show that a controllable spin splitting can be reached.

Halide organic–inorganic perovskites are hybrid materials and often show important distortions from the ideal octahedron. These deformations are a contributing factor to the different properties of this class of perovskite.[58,59] However, if the loss of inversion symmetry is a requirement for the spin splitting, we stress that the loss of too many symmetry operations can lead to an unusable Rashba effect with uncharacteristic spin rotations.

Non-centrosymmetric Structures. As a first case, we consider the methylammonium lead iodide perovskite, $CH_3NH_3PbI_3$, in the *P4mm* crystal group.[60] Starting from the $Pm\bar{3}m$ structure, it corresponds to a simple translation of the ions along the *z* axis. The resulting structure shows a C_{4v} point group. The C_4 axis lies along the [001] crystallographic direction. Thus, [001] naturally defines the special quantization axis $\mathbf{k}_\perp$, $\mathbf{k}_\parallel$ is contained in the plane that can for instance be defined by the two vectors $\mathbf{k}_x$ = [100] and $\mathbf{k}_y$ = [010]. The critical point $\mathbf{k}_0$ is the point A (1/2, 1/2, 1/2). Figure 3a displays the band structure of $CH_3NH_3PbI_3$ calculated with and without SOC in the $\mathbf{k}_\parallel$ plane. The SOC has three major contributions: (i) the gap is greatly reduced, (ii) the conduction band minimum (CBM) and the valence band maximum (VBM) are displaced away from A, and (iii) the conduction and valence bands are split away from A. The four resulting bands present similar spin textures (Figure 3d) with spins orthogonal to the crystal momenta.

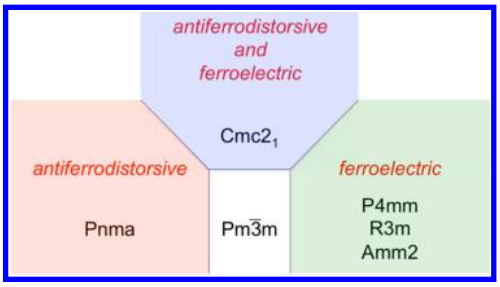

Figure 2. Phase transitions from $Pm\bar{3}m$.

This pure Rashba picture is consistent with the predicted form of the spin–orbit Hamiltonian for a C_{4v} symmetry.[53] The apparent absence of deviation from the model (Figure 1b) indicates weak or vanishing contributions from cubic terms. From the momentum shift, k_R, and the energy splitting, ΔE, we deduce the strength of the Rashba effect, $\lambda_R = \Delta E/(2k_R)$, and find a Rashba coefficient of λ_R^{CBM} = 3.76 eV·Å for the conduction band and λ_R^{VBM} = 3.71 eV·Å for the valence band. These Rashba splittings are of the same order of magnitude as the largest splittings experimentally observed in bulk materials, for example, λ_R = 3.80 eV·Å for BiTeI,[26,27] or surface alloys, for example, λ_R = 3.05 eV·Å for Bi/Ag(111).[31]

From the $Pm\bar{3}m$ reference structure, simultaneous translations of the ions along the three crystallographic axes lead to an *R3m* structure. The corresponding point symmetry is C_{3v}. In the case of methylammonium

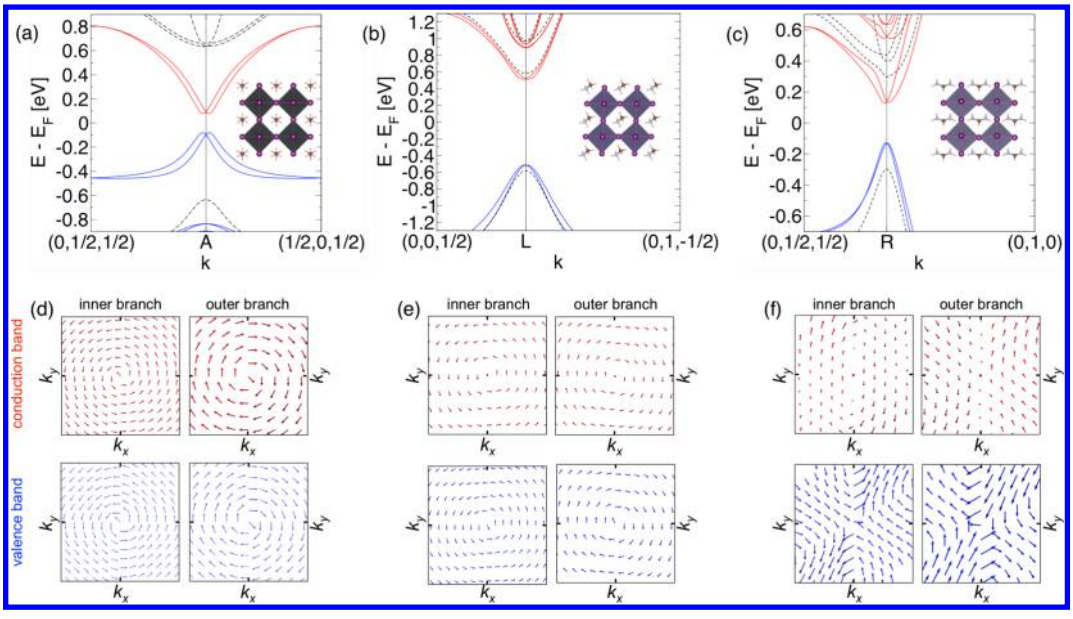

Figure 3. Hybrid organic–inorganic halide perovskites crystallized in phases corresponding to a ferroelectric phase transition from $Pm\bar{3}m$. (a) Band structure and structure (insert) of $CH_3NH_3PbI_3$ in the *P4mm* phase. Blue and red lines stand for the occupied and unoccupied bands, respectively, for a calculation including SOC. Black dashed lines are the results without SOC. (b) Same for $CH_3NH_3GeI_3$ in the *R3m* phase. (c) Same for $CH(NH_2)_2SnI_3$ crystallized in the *Amm2* group. (d, e, f) Spin textures for the inner and outer branches for both occupied and unoccupied bands of $CH_3NH_3PbI_3$, $CH_3NH_3GeI_3$, and $CH(NH_2)_2SnI_3$, respectively.

germanium iodide, $CH_3NH_3GeI_3$,[60] the C_3 quantization axis ($\mathbf{k}_\perp$) is parallel to the [111] crystallographic direction. Hence, the relevant plane to observe a Rashba-like spin splitting ($\mathbf{k}_\parallel$) contains the $[1\bar{1}0]$ and $[11\bar{2}]$ directions. In Figure 3b, we plot the band structure following the relevant path around the critical point *L* (−1/2, 1/2, 1/2). Once more, splittings are observed for conduction and valence bands. The effect appears more pronounced in the conduction band. The spin textures (Figure 3e) are again characteristic of a pure Rashba spin splitting as predicted by the symmetry reduction of the $\mathbf{k}\cdot\mathbf{p}$ Hamiltonian in the case of a C_{3v} point group.[53] There is no measurable out-of-plane component of the spin vectors, as it was for $CH_3NH_3PbI_3$. We extract again the values of λ_R and find λ_R^{CBM} = 0.89 eV·Å, λ_R^{VBM} = 0.45 eV·Å. These values are much weaker than those obtained for $CH_3NH_3PbI_3$ but still sizable. The lowering of the Rashba spin splitting is expected because the atomic SOC splitting is much more important for the Pb^{2+} ion than for Ge^{2+} (1.75 vs 0.22 eV).[59]

$CH_3NH_3GeCl_3$ also crystallizes in a *R*3*m* structure.[56] With chlorine, the structure is more distorted than in the case of iodine (Figure S1a in Supporting Information). The band structure remains similar to a band splitting in conduction and valence bands (Figure S1b). The difference is quantitative with λ_R^{CBM} = 1.18 eV·Å and λ_R^{VBM} = 0.23 eV·Å. The Rashba effect appears stronger in the conduction band than in the case of $CH_3NH_3GeI_3$. The Rashba effect is thus resilient to important lattice distortions. However, in addition to the expected shape, the spin textures show important out-of-plane components even for small values of the momentum (Figure S1c,d). This strain-induced alteration of electronic eigenvectors is a detrimental effect that may hinder the definition of purely intricate spin states for device applications (vide infra).

As a final example of ferroelectric structures, we investigate $CH(NH_2)_2SnI_3$ in the *Amm*2 group.[49,61] It corresponds to twin translations of the ions along the *x* and *y* directions. The resulting point group symmetry is C_{2v}, with the C_2 axis in the [011] direction. We plot the band structure around *R* (1/2, 1/2, 1/2) probing the [100] and $[01\bar{1}]$ directions. The splitting of bands occurs for both the conduction and valence bands. However, the spin textures close to the CBM and VBM for the inner and outer branches (Figure 3f) are very different from the previous examples, even if no out-of-plane contribution can be extracted. It does not correspond to any of the limiting cases presented in Figure 1. As detailed previously, a system belonging to C_{2v} symmetry can exhibit both Rashba and Dresselhaus terms, eq 2. Using eqs 3 and 10 and the spin orientations for different momentum, we get the relative contributions of both effects: λ_D^{CBM} = 2.59 eV·Å and λ_R^{CBM} = 0.50 eV·Å. Our results are in good agreement with previous GW calculations (where the Rashba and Dresselhaus parameters are computed as $\Delta E/k_R$, accounting for the factor of 2 discrepancy between their and our results).[49] The effect is too weak in the valence band, and no parameter can be computationally assessed in this case.

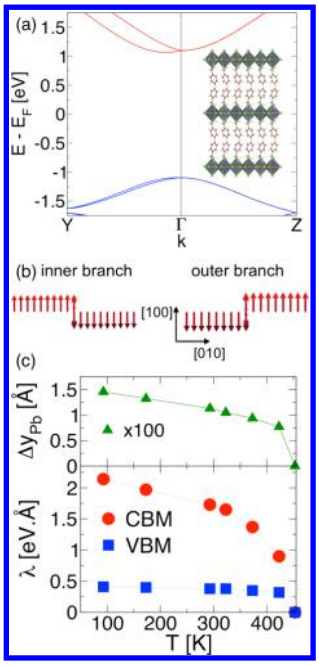

Figure 4. (a) Band structure of Bz_2PbCl_4 in the low temperature $Cmc2_1$ phase, computed with SOC. Blue and red bands correspond to occupied and unoccupied bands, respectively. (b) Spin textures for the inner and outer branches of the conduction band. (c) Temperature dependence of the Pb displacement along *y* (see text) and computed Rashba parameters for the conduction and valence bands.

Ferroelectric Transitions: Temperature-Controlled Rashba Spin Splitting. The ideal reference structure for bulk 2D hybrid perovskites corresponds to the D_{4h} point group.[62] However, high temperature centrosymmetric crystal phases of 2D hybrid perovskites usually exhibit a cell doubling in a plane perpendicular to the stacking axis, associated with antiferrodistorsive tilts of the octahedra. This lattice distortion leads to a reduction of the point group symmetry from D_{4h} to D_{2h} and a BZ folding from the M point at the BZ boundary to the Γ point at the BZ center. Such a structure is observed at high temperature for the 2D hybrid perovskite Bz_2PbCl_4 (Bz = benzylammonium),[63,64] which crystallizes in a *Cmca* (no. 64) centrosymmetric phase.[64] The structure is layered with slabs of single octahedra sandwiched by slabs of organic cations (Figure 4). Below *T* = 438 K, the crystal undergoes a ferroelectric phase transition to a $Cmc2_1$ non-centrosymmetric structure.

In the low temperature phase, the C_2 quantization axis is along the [001] crystallographic direction, and thus no spin splitting occurs on the $\Gamma \rightarrow Z$ path (Figure 4a). Following the previous scheme, $\mathbf{k}_\parallel$ should be defined by [100] and [001]. Because [100] corresponds to the stacking direction, there is no dispersion

of the bands due to the organic part in this direction.[9] The spin splitting can be observed following $\Gamma \rightarrow Y$. This situation notably differs from the Rashba effect in conventional semiconductor QW and heterostructures where the stacking and quantization axes coincide. Therefore, the problem becomes analogous to a 1D problem with contributions involving only k_y:

$$\mathscr{H}(\mathbf{k}_x) = -\lambda_R k_y \sigma_x + \lambda_D k_y \sigma_y \quad (11)$$

The eigenvalues and eigenvectors become

$$E_{RD\pm}(k_y) = \frac{\hbar {k_y}^2}{2m} \pm \sqrt{({\lambda_D}^2 + {\lambda_R}^2){k_y}^2} \quad (12)$$

$$\Psi_{1D\pm} \propto \begin{pmatrix} \mp \dfrac{\lambda_R - i\lambda_D}{\sqrt{{\lambda_R}^2 + {\lambda_D}^2}} \dfrac{k_y}{|k_y|} \\ 1 \end{pmatrix} \quad (13)$$

and the spin textures read

$$\langle \sigma \rangle_{\pm} \propto \begin{pmatrix} \mp \dfrac{k_y}{|k_y|} \\ 0 \\ 0 \end{pmatrix} \quad (14)$$

Only one spin component is obtained along the stacking direction. Clearly, there is no differential impact on the observables (band splitting and σ expectation values) of the Rashba vs Dresselhaus nature of the spin splitting. Then, one can note λ, the effective amplitude:

$$\lambda = \frac{\Delta E_{RD}(k_y)}{2k_y} \quad (15)$$

The band structure calculated for the low-temperature structure (93 K) of Bz_2PbCl_4 (Figure 4a) shows a large effect on the conduction band (λ^{CBM} = 2.14 eV·Å) and much weaker on the valence band (λ^{VBM} = 0.41 eV·Å). The spin textures for both branches of the conduction band (Figure 4b) display the expected features with a single component whatever the momentum.

Recently, Liao et al. have characterized the crystal structure of Bz_2PbCl_4 at various temperatures.[64] The crystal remains in the $Cmc2_1$ group for temperatures from 93 K up to 423 K. The high temperature structure (453 K) presents a *Cmca* symmetry, that is, a D_{2h} point group, and, therefore, does not exhibit spin splitting. We compute the electronic structure for each experimental structure and determine the evolution of the Rashba parameter λ with temperature (Figure 4c). The temperature induced variation of the Rashba parameter can be related to the order parameter of the *Cmca* (D_{2h}) to $Cmc2_1$ (C_{2v}) ferroelectric phase transition. This order parameter corresponds to the B_{1u} irreducible representation (IR) of the D_{2h} point group and to a polarization along the C_2 axis ([001] direction). The analysis of the *Cmca* phonon modes shows that the B_{1u} IR appears in both the mechanical representations of the Pb and Cl atoms, with a parallel motions of two Pb (or Cl) atoms along the *z* axis and antiparallel motions along the *y* axis. The low temperature $Cmc2_1$ phase can thus be partly described as a displacive distortion from the *Cmca* phase with the corresponding atomic displacements in the inorganic layer from their high temperature positions. We shall point out that the phase transition is also related to an order−disorder character in relation with the disordered orientations of the organic molecules in the *Cmca* phase. The splitting in the valence band is weakly affected by the structural changes occurring from 93 to 423 K with a λ^{VBM} slowly varying from 0.41 eV·Å to 0.32 eV·Å. On the other hand, the Rashba effect in the conduction bands is stronger. This smooth variation is related to the atomic displacement in the low temperature phase. Indeed, the decrease from 2.14 eV·Å to 0.90 eV·Å can be traced back to structural characteristics such as the displacement of Pb atoms along *y* (Figure 4, Figures S2 and S3).

The effect of octahedron distortions ($CH_3NH_3GeCl_3$) and of the in-plane and out-of-plane tilts (Bz_2PbCl_4) have illustrated the delicate balance of symmetry/asymmetry required to observe a Rashba effect in this class of hybrid materials. In the following, we consider the case of spin splitting induced by an external electric field.

Field-Controlled Rashba Spin Splitting. In this section, we examine electric field-controlled Rashba splitting starting from 3D hybrid perovskites. An electric field applied to the $Pm\bar{3}m$ reference structure corresponds to a Γ_4^- perturbation and may lead to one of the three ferroelectric distortions already described in the first part. However, given that the organic cations are dynamically disordered in the $Pm\bar{3}m$, we perform DFT simulations of this effect for the low-temperature *Pnma* structure, which corresponds to an antiferrodistorsive distortion of the $Pm\bar{3}m$ phase. This centrosymmetric structure is often encountered among hybrid organic−inorganic perovskites[56,57,65] and corresponds to the low-temperature phase of $CH_3NH_3PbI_3$.[65] The *Pnma* space group corresponds to a D_{2h} point symmetry. Therefore, no Rashba effect can be expected in this case. Nevertheless, when a transverse external electric field, $\mathbf{E}_{ext}$, is applied, the inversion symmetry is lost and a spin splitting is expected to show up. The same goes for the cubic $Pm\bar{3}m$ or tetragonal *I*4/*mcm* phases.

Control of spin splitting, and thus of the Rashba parameter, by a gate voltage, that is, an external electric field, has been under intense investigation since the mid-1990s.[21−23,32] In the early 2000s, theoretical investigations significantly contributed to rationalize the effect. In particular, tight-binding models have provided essential support to evaluate the Rashba parameter as a function of microscopic quantities.[15,66−69] Recently, Kim and co-workers have adapted such models to hybrid organic−inorganic perovskites in the case of non-centrosymmetric structures, but without

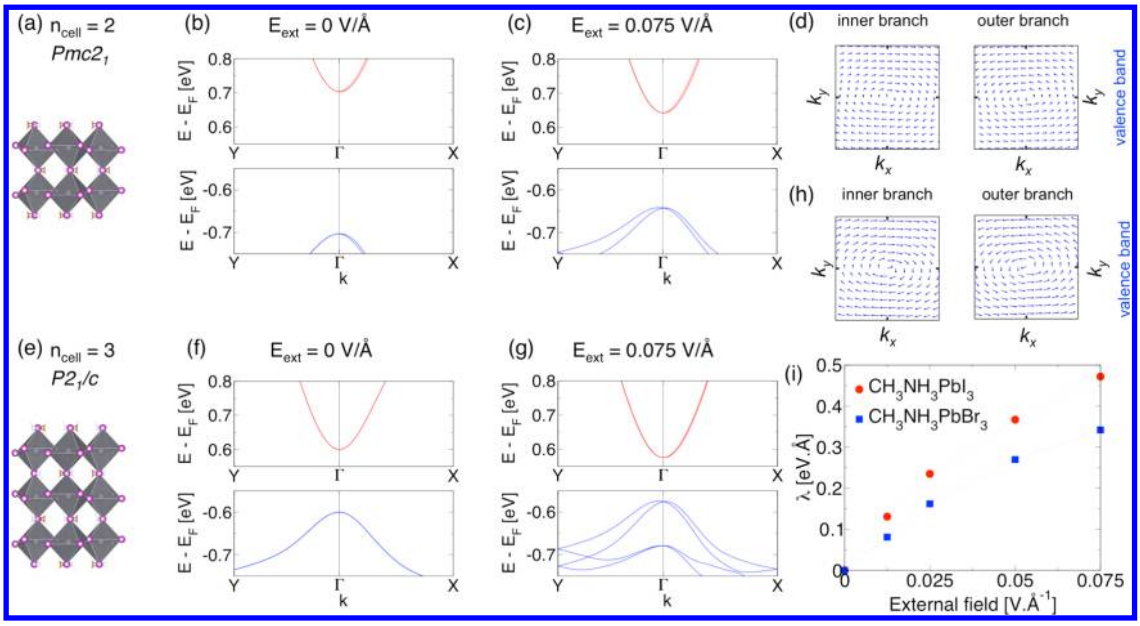

Figure 5. Electric field induced spin splitting in slabs of $CH_3NH_3PbI_3$. The original bulk crystal group is *Pnma*. Slabs with even and odd thickness (n_{cell}) exhibit $Pmc2_1$ and $P2_1/c$ symmetry, respectively. (a,e) Structures of slabs of $CH_3NH_3PbI_3$ with n_{cell} = 2 and 3, respectively. Pb, I, N, C, and H are depicted in gray, purple, blue, brown, and white, respectively. (b,f) Corresponding band structure computed with SOC. Blue and red bands correspond to occupied and unoccupied band, respectively. A small splitting is observed in the case of n_{cell} = 2. (c, g) Same with the application of an external electric field E_{ext} = 0.075 V Å^{-1}. A splitting is observed with corresponding spin textures depicted in panels d and h for the valence bands. (i) Rashba parameter, λ_R (eV·Å), as a function of the applied electric field, E_{ext} (V Å^{-1}) for $CH_3NH_3PbI_3$ (red circles) and $CH_3NH_3PbBr_3$ (blue squares).

considering an external electric field.[46] Although the complete description of such models is beyond the scope of this work, let us recall here that they describe a Rashba parameter that depends linearly on the atomic SOC and on the effective potential gradient and decreases with an increasing band gap.

In order to apply the electric field, we start from the bulk structure of $CH_3NH_3PbI_3$ in the *Pnma* phase and construct slabs terminated by the [010] surface, containing n_{cell} octahedra in the packing direction. Two cases occur: (i) n_{cell} is even (Figure 5a), and the resulting structure belongs to the non-centrosymmetric group $Pmc2_1$ (no. 26) corresponding to the C_{2v} point group; (ii) n_{cell} is odd (Figure 5e), and the structure presents a centrosymmetric $P2_1/c$ (no. 14) space group corresponding to the C_{2h} point group. The consequence of this odd/even effect is illustrated by the band structures calculated for slabs with n_{cell} = 2 and 3 (Figure 5b,f) around Γ in both in-plane directions [100] and [010]. Indeed, no splitting is observed for the conduction and valence bands when n_{cell} = 3, whereas n_{cell} = 2 leads to a small splitting along $\Gamma \rightarrow X$ (1/2, 0, 0). However, this is not the case when going to thicker slabs: for slabs with $n_{cell} \geq 4$, no splitting is retrieved in our calculations.

A spin splitting is observed when applying a transverse electric field, $\mathbf{E}_{ext}$ (Figure 5c,g). This effect is almost null in the conduction band but can lead to λ_R of nearly 0.5 eV·Å in the valence band. Noteworthy, whatever the thickness of the slab, bands close to the gap are not surface states and the splitting is not a difference between up and down faces of the slab. The spin textures of the inner and outer branches of the valence band are similar for odd and even cases (Figure 5d,h) and correspond to Rashba spin splittings.

We monitor the evolution of the valence band Rashba parameter λ_R with the amplitude of the applied transverse electric field, $\mathbf{E}_{ext}$ (Figure 5i). Let us note that for $n_{cell} \geq 7$, the bulk gap is recovered and the Rashba parameter is no longer dependent on the thickness of the slab (Figure S4). In other words, a bulk-like behavior is described. λ_R owes its increase to two electric field effects: (i) the induced asymmetry and (ii) the band gap modulation due to the Stark effect that tends to close the gap. We observe a linear dependence of λ_R with respect to the external field, $\mathbf{E}_{ext}$, for weak fields. In addition to the external field, the amplitude of the Rashba parameter is affected by the atomic SOC and by the original (no field) band gap of the materials. This can be verified by applying the same procedure to $CH_3NH_3PbBr_3$ in the same *Pnma* phase.[70] In this way, the atomic SOC is almost constant, and only the band gap is modified. It varies from 1.03 eV for $CH_3NH_3PbI_3$ to 1.38 eV for $CH_3NH_3PbBr_3$ in our DFT+SOC calculations, whose underestimation of semiconductor band gaps is well-known.[10,11,47,71] We find a 28% diminution of λ_R when replacing I by Br that is in line with the 33% increase of the band gap. When the field becomes stronger, a bending is observed that might be the related to higher order terms.

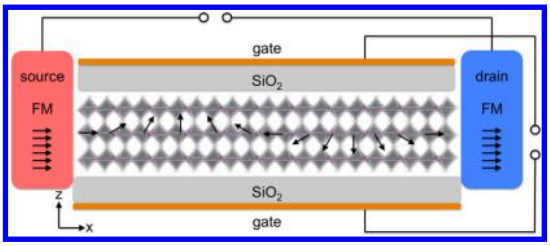

Figure 6. Scheme of a sFET as proposed by Datta and Das[72] based on hybrid organic−inorganic perovskites with a representation of the spin precession from the source to the drain.

The aspiration for a field-controlled Rashba spin splitting was first motivated by the design of a spin FET following the original scheme proposed by Datta and Das in 1990 (Figure 6).[72] In this setup, the electron spins precess under the influence of the Rashba or Dresselhaus coupling or both. Then, by tuning the amplitude of the effect, one will act on the phase, and the electron leaving the source can reach the drain in or out-of-phase. After the very first observations of tunable Rashba splitting,[21−23] several examples of devices have been produced[38,39,73,74] or proposed on the basis of theoretical inspections.[75,76] More elaborated devices have been proposed based on the same principle, adding a transverse magnetic field to the electric one and using more than one site for SOC effect. In this manner, a perfect spin filter can be achieved.[77−79]

Based on our findings, a similar scheme can be proposed using, as an example, the low cost hybrid organic−inorganic perovskite $CH_3NH_3PbI_3$, in the *Pnma* structure. Contrary to the previous examples,[38,39,73−79] the suggested setup presents no manifestation of the SOC in terms of spin splitting (λ_R = 0 eV·Å) when the electric field is switched off, which makes less delicate the tuning of the source−drain distance and of the amplitude of the transverse field.

Let us consider the case of ferromagnetic source and drain with magnetizations along $+x$ being also the direction of propagation of the electron. In the semiconductor part of the transistor we find the quantization axis along z, which is the orientation of the gate. The electron is injected with a magnetization along x, i.e. presents a spinor of the form $1/\sqrt{2}$ (1,1), with an energy ϵ. In the case of a Rashba spin splitting, from eq 7, the basis on which the spinors are then decomposed is given by

$$|+\rangle = \frac{1}{\sqrt{2}}\begin{pmatrix} -i \\ 1 \end{pmatrix} \quad \text{and} \quad |-\rangle = \frac{1}{\sqrt{2}}\begin{pmatrix} +i \\ 1 \end{pmatrix} \tag{16}$$

The $+x$ oriented spin is then expressed as

$$|+x\rangle = \frac{1}{2}[(1+i)|+\rangle + (1-i)|-\rangle] \tag{17}$$

$|+\rangle$ and $|-\rangle$ eigenstates propagate with momentum k_+ and k_- given by eq 3, with (Figure 1a)

$$\Delta k = k_- - k_+ = \frac{2m}{\hbar^2}\lambda_R \tag{18}$$

and the wave function of the propagating electron is given by

$$\Psi(x) = \frac{1}{2}\left[(1+i)\frac{e^{ik_+x}}{\sqrt{2}}\begin{pmatrix} -i \\ 1 \end{pmatrix} + (1-i)\frac{e^{ik_-x}}{\sqrt{2}}\begin{pmatrix} +i \\ 1 \end{pmatrix}\right] \tag{19}$$

and the expectation value $\langle \boldsymbol{\sigma} \rangle$ at the distance L is

$$\langle \sigma \rangle \propto \begin{pmatrix} \cos(\Delta k \cdot L) \\ 0 \\ -\sin(\Delta k \cdot L) \end{pmatrix} \tag{20}$$

One can see that the spin precesses in the (x,z) plane. To obtain a spin anti-align (off-state) with the magnetization of the drain (Figure 6), the length should be tuned such as

$$\Delta k \cdot L_{off} = \left(n + \frac{1}{2}\right)\pi \tag{21}$$

where n is an integer. And thus,

$$L_{off} = \left(n + \frac{1}{2}\right)\frac{\pi\hbar^2}{m\lambda_R} \tag{22}$$

If we consider a device with a thickness of 10 nm, then an applied field of 0.0125 V·Å corresponds to a gate voltage of 1.25 V and a λ_R of about 0.1 eV·Å. Then, the lengths corresponding to off-states are 12 nm (n = 0), 36 nm (n = 1), etc.

We stress that these lengths are qualitative estimates. In fact, a quantitative description of spin transport is more complex and entails further developments. For instance, the investigation of spin polarization in these materials remains to be conducted. It requires the use of the full multiband Luttinger Hamiltonian instead of the effective 2 × 2 one.[15,18,80−83] Concurrently, spin relaxation phenomena, which necessarily occur and would limit the spin diffusion length, should also be taken into account.[42] Recent experimental data on solution-processed polycrystalline hybrid perovskites have already shown spin relaxation lifetimes of 7 ps for holes and electrons, suggesting that longer spin diffusion could be reached with crystalline samples.[51]

CONCLUSION

Hybrid organic−inorganic perovskite have become extremely popular over the last five years in the field of photovoltaics. In this respect, they were initially regarded as dyes and, as such, related to organometallic dyes. However, these materials were first considered, in their 2D form, for applications in optoelectronics and related to conventional semiconductors.[6−8] Here we pursue in line with this and conduct a survey of the Rashba and Dresselhaus effects in these atypical semiconductors. We have recalled the general conditions to observe Rashba and Dresselhaus spin splittings based on symmetry analysis and $\mathbf{k}\cdot\mathbf{p}$ expansion. We apply this

approach to several examples in non-centrosymmetric structures presenting C_{4v}, C_{3v}, and C_{2v} symmetries. Even for Ge-based compounds we find Rashba parameters of nearly 1 eV·Å, proving that despite the important distortions caused by the organic cation, the SOC effect prevails. By means of a 2D non-centrosymmetric structure, we show how the amplitude of the splitting can be monitored with temperature, as a result of the continuous polarization of the crystal structure from high to low temperatures. Finally we inspect the case of centrosymmetric structure exhibiting a Rashba spin splitting under the influence of a transverse electric field. The possibility to control the spin precession in the material thanks to a gate voltage constitutes the base for a hybrid organic−inorganic perovskite-based spin FET.

METHODS

First-principles calculations are based on DFT as implemented in the SIESTA package.[84,85] Calculations have been carried out with the GGA functional in the PBE form,[86] Troullier−Martins pseudopotentials,[87] and a basis set of finite-range numerical pseudoatomic orbitals for the valence wave functions.[88] Structure relaxation and electronic structure calculations have been done using double-ζ polarized basis sets.[88] In our calculations, SOC is taken into account through the on-site approximation as proposed by Fernández-Seivane et al.[89] In all cases, an energy cutoff of 150 Ry for real-space mesh size has been used. In the case of $CH_3NH_3PbI_3$ and $CH_3NH_3PbBr_3$ slabs, the bulk has been relaxed, but no subsequent geometry relaxation has been conducted on slabs. This strategy allows us to stay as close as possible to the bulk behavior of the materials.

We have repeated selected calculations using plane wave basis sets and the projected augmented wave method as implemented in VASP.[90,91] We have used the same structures relaxed by SIESTA with the same exchange and correlation scheme and k-points sampling. The cutoff energy has been chosen between 300 and 500 eV depending on the structure. The results obtained with VASP confirm the main features previously obtained by SIESTA. We have also used the VASP code to obtain the spin textures.

Conflict of Interest: The authors declare no competing financial interest.

Acknowledgment. This work has been supported by Cellule Energie du CNRS (SOLHYBTRANS Project) and University of Rennes 1 (Action Incitative, Défis Scientifiques Emergents 2015). J.E.'s work is supported by the *Fondation d'entreprises banque Populaire de l'Ouest* under Grant PEROPHOT 2015. ICN2 acknowledges support from the Severo Ochoa Program (MINECO, Grant SEV-2013-0295). J.E. and C.K. thank R. Winkler for fruitful discussions. We gratefully acknowledge Prof. R.-G. Xiong for providing Bz_2PbCl_4 crystallographic data.[64]

Supporting Information Available: The Supporting Information is available free of charge on the ACS Publications website at DOI: 10.1021/acsnano.5b04409.

Additional results on $CH_3NH_3GeCl_3$, Bz_2PbCl_4 and $CH_3NH_3PbI_3$ (PDF)

REFERENCES AND NOTES

1. Kojima, A.; Teshima, K.; Shirai, Y.; Miyasaka, T. Organometal Halide Perovskites as Visible-Light Sensitizers for Photovoltaic Cells. *J. Am. Chem. Soc.* **2009**, *131*, 6050–6051.
2. Zhou, H.; Chen, Q.; Li, G.; Luo, S.; Song, T.; Duan, H.-S.; Hong, Z.; You, J.; Liu, Y.; Yang, Y. Interface Engineering of Highly Efficient Perovskite Solar Cells. *Science* **2014**, *345*, 542–546.
3. Snaith, H. J. Perovskites: The Emergence of a New Era for Low-Cost, High-Efficiency Solar Cells. *J. Phys. Chem. Lett.* **2013**, *4*, 3623–3630.
4. Green, M. A.; Ho-Baillie, A.; Snaith, H. J. The Emergence of Perovskite Solar Cells. *Nat. Photonics* **2014**, *8*, 506–514.
5. Grätzel, M. The Light and Shade of Perovskite Solar Cells. *Nat. Mater.* **2014**, *13*, 838–842.
6. Mitzi, D. B.; Feild, C. A.; Harrison, W. T. A.; Guloy, A. M. Conducting Tin Halides with a Layered Organic-Based Perovskite Structure. *Nature* **1994**, *369*, 467–469.
7. Mitzi, D. B.; Wang, S.; Feild, C. A.; Chess, C. A.; Guloy, A. M. Conducting Layered Organic-inorganic Halides Containing 110-Oriented Perovskite Sheets. *Science* **1995**, *267*, 1473–1476.
8. Kagan, C. R.; Mitzi, D. B.; Dimitrakopoulos, C. D. Organic-Inorganic Hybrid Materials as Semiconducting Channels in Thin-Film Field-Effect Transistors. *Science* **1999**, *286*, 945–947.
9. Even, J.; Pedesseau, L.; Dupertuis, M.-A.; Jancu, J.-M.; Katan, C. Electronic Model for Self-Assembled Hybrid Organic/Perovskite Semiconductors: Reverse Band Edge Electronic States Ordering and Spin-Orbit Coupling. *Phys. Rev. B: Condens. Matter Mater. Phys.* **2012**, *86*, 205301.
10. Even, J.; Pedesseau, L.; Jancu, J.-M.; Katan, C. Importance of Spin-Orbit Coupling in Hybrid Organic/Inorganic Perovskites for Photovoltaic Applications. *J. Phys. Chem. Lett.* **2013**, *4*, 2999–3005.
11. Even, J.; Pedesseau, L.; Jancu, J.-M.; Katan, C. DFT and k.p Modelling of the Phase Transitions of Lead and Tin Halide Perovskites for Photovoltaic Cells. *Phys. Status Solidi RRL* **2014**, *8*, 31–35.
12. Dresselhaus, G. Spin-Orbit Coupling Effects in Zinc Blende Structures. *Phys. Rev.* **1955**, *100*, 580–586.
13. Rashba, E. I. Properties of Semiconductors with an Extremum Loop. 1. Cyclotron and Combinational Resonance in a Magnetic Field Perpendicular to the Plane of the Loop. *Sov. Phys. Solid State* **1960**, *2*, 1224–1238.
14. Bychkov, Y. A.; Rashba, E. I. Properties of a 2D Electron Gas with Lifted Spectral Degeneracy. *JETP Lett.* **1984**, *39*, 78–81.
15. Winkler, R. *Spin-Orbit Coupling Effects in Two-Dimensional Electron and Hole Systems*; Springer: Berlin, 2003.
16. Dil, J. H. Spin and Angle Resolved Photoemission on Non-Magnetic Low-Dimensional Systems. *J. Phys.: Condens. Matter* **2009**, *21*, 403001.
17. Ganichev, S. D.; Golub, L. E. Interplay of Rashba/Dresselhaus Spin Splittings Probed by Photogalvanic Spectroscopy - A Review. *Phys. Status Solidi B* **2014**, *251*, 1801–1823.
18. Zhang, X.; Liu, Q.; Luo, J.-W.; Freeman, A. J.; Zunger, A. Hidden Spin Polarization in Inversion-Symmetric Bulk Crystals. *Nat. Phys.* **2014**, *10*, 387–393.
19. Bihlmayer, G.; Rader, O.; Winkler, R. Focus on the Rashba Effect. *New J. Phys.* **2015**, *17*, 050202.
20. Lommer, G.; Malcher, F.; Rossler, U. Spin Splitting in Semiconductor Heterostructures for B→0. *Phys. Rev. Lett.* **1988**, *60*, 728–731.
21. Nitta, J.; Akazaki, T.; Takayanagi, H.; Enoki, T. Gate Control of Spin-Orbit Interaction in an Inverted $In_{0.53}Ga_{0.47}As/In_{0.52}Al_{0.48}As$ Heterostructure. *Phys. Rev. Lett.* **1997**, *78*, 1335–1338.
22. Schultz, M.; Heinrichs, F.; Merkt, U.; Colin, T.; Skauli, T.; Løvold, S. Rashba Spin Splitting in a Gated HgTe Quantum Well. *Semicond. Sci. Technol.* **1996**, *11*, 1168–1172.
23. Engels, G.; Lange, J.; SchäPers, T.; Lüth, H. Experimental and Theoretical Approach to Spin Splitting in Modulation-Doped $In_xGa_{1-x}As/InP$ Quantum Wells for $B\rightarrow 0$. *Phys. Rev. B: Condens. Matter Mater. Phys.* **1997**, *55*, R1958–R1961.

24. Balocchi, A.; Amand, T.; Wang, G.; Liu, B. L.; Renucci, P.; Duong, Q. H.; Marie, X. Electric Field Dependence of the Spin Relaxation Anisotropy in (111) GaAs/AlGaAs Quantum Wells. *New J. Phys.* **2013**, *15*, 095016.
25. Wang, G.; Balocchi, A.; Poshakinskiy, A. V.; Zhu, C. R.; Tarasenko, S. A.; Amand, T.; Liu, B. L.; Marie, X. Magnetic Field Effect on Electron Spin Dynamics in (110) GaAs Quantum Wells. *New J. Phys.* **2014**, *16*, 045008.
26. Ishizaka, K.; Bahramy, M. S.; Murakawa, H.; Sakano, M.; Shimojima, T.; Sonobe, T.; Koizumi, K.; Shin, S.; Miyahara, H.; Kimura, A.; et al. Giant Rashba-type Spin Splitting in Bulk BiTeI. *Nat. Mater.* **2011**, *10*, 521–526.
27. Eremeev, S. V.; Nechaev, I. A.; Koroteev, Y. M.; Echenique, P. M.; Chulkov, E. V. Ideal Two-Dimensional Electron Systems with a Giant Rashba-Type Spin Splitting in Real Materials: Surfaces of Bismuth Tellurohalides. *Phys. Rev. Lett.* **2012**, *108*, 246802.
28. Ideue, T.; Checkelsky, J. G.; Bahramy, M. S.; Murakawa, H.; Kaneko, Y.; Nagaosa, N.; Tokura, Y. Pressure Variation of Rashba Spin Splitting Toward Topological Transition in the Polar Semiconductor BiTeI. *Phys. Rev. B: Condens. Matter Mater. Phys.* **2014**, *90*, 161107(R).
29. LaShell, S.; McDougall, B. A.; Jensen, E. Spin Splitting of an Au(111) Surface State Band Observed with Angle Resolved Photoelectron Spectroscopy. *Phys. Rev. Lett.* **1996**, *77*, 3419–3422.
30. Koroteev, Y. M.; Bihlmayer, G.; Gayone, J. E.; Chulkov, E. V.; Blügel, S.; Echenique, P. M.; Hofmann, P. Strong Spin-Orbit Splitting on Bi Surfaces. *Phys. Rev. Lett.* **2004**, *93*, 046403.
31. Ast, C. R.; Henk, J.; Ernst, A.; Moreschini, L.; Falub, M. C.; Pacilé, D.; Bruno, P.; Kern, K.; Grioni, M. Giant Spin Splitting through Surface Alloying. *Phys. Rev. Lett.* **2007**, *98*, 186807.
32. Takayama, A.; Sato, T.; Souma, S.; Oguchi, T.; Takahashi, T. Tunable Spin Polarization in Bismuth Ultrathin Film on Si(111). *Nano Lett.* **2012**, *12*, 1776–1779.
33. Bianchi, M.; Hatch, R. C.; Li, Z.; Hofmann, P.; Song, F.; Mi, J.; Iversen, B. B.; Abd El-Fattah, M.; Löptien, P.; Zhou, L.; et al. Robust Surface Doping of Bi_2Se_3 by Rubidium Intercalation. *ACS Nano* **2012**, *6*, 7009–7015.
34. Eremeev, S. V.; Rusinov, I. P.; Nechaev, I. A.; Chulkov, E. V. Rashba Split Surface States in BiTeBr. *New J. Phys.* **2013**, *15*, 075015.
35. Santander-Syro, A. F.; Fortuna, F.; Bareille, C.; Rödel, T. C.; Landolt, G.; Plumb, N. C.; Dil, J. H.; Radović, M. Giant Spin Splitting of the Two-Dimensional Electron Gas at the Surface of $SrTiO_3$. *Nat. Mater.* **2014**, *13*, 1085–1090.
36. Wang, E.; Tang, P.; Wan, G.; Fedorov, A. V.; Miotkowski, I.; Chen, Y. P.; Duan, W.; Zhou, S. Robust Gapless Surface State and Rashba-Splitting Bands upon Surface Deposition of Magnetic Cr on Bi_2Se_3. *Nano Lett.* **2015**, *15*, 2031–2036.
37. Banerjee, A.; Dogan, F.; Heo, J.; Manchon, A.; Guo, W.; Bhattacharya, P. Spin Relaxation in InGaN Quantum Disks in GaN Nanowires. *Nano Lett.* **2011**, *11*, 5396–5400.
38. Liang, D.; Gao, X. P. A. Strong Tuning of Rashba Spin-Orbit Interaction in Single InAs Nanowires. *Nano Lett.* **2012**, *12*, 3263–3267.
39. Zhang, S.; Tang, N.; Jin, W.; Duan, J.; He, X.; Rong, X.; He, C.; Zhang, L.; Qin, X.; Dai, L.; et al. Generation of Rashba Spin-Orbit Coupling in CdSe Nanowire by Ionic Liquid Gate. *Nano Lett.* **2015**, *15*, 1152–1157.
40. Gregg, J. F.; Petej, I.; Jouguelet, E.; Dennis, C. Spin Electronics - a Review. *J. Phys. D: Appl. Phys.* **2002**, *35*, R121–R155.
41. Jansen, R. The Spin-Valve Transistor: a Review and Outlook. *J. Phys. D: Appl. Phys.* **2003**, *36*, R289–R308.
42. Zutić, I.; Fabian, J.; Das Sarma, S. Spintronics: Fundamentals and Applications. *Rev. Mod. Phys.* **2004**, *76*, 323–410.
43. Jansen, R. Silicon Spintronics. *Nat. Mater.* **2012**, *11*, 400–408.
44. Sau, J. D.; Lutchyn, R. M.; Tewari, S.; Das Sarma, S. Generic New Platform for Topological Quantum Computation Using Semiconductor Heterostructures. *Phys. Rev. Lett.* **2010**, *104*, 040502.
45. Alicea, J.; Oreg, Y.; Refael, G.; von Oppen, F.; Fisher, M. P. A. Non-Abelian Statistics and Topological Quantum Information Processing in 1D Wire Networks. *Nat. Phys.* **2011**, *7*, 412–417.
46. Kim, M.; Im, J.; Freeman, A. J.; Ihm, J.; Jin, H. Switchable S = 1/2 and J = 1/2 Rashba bands in Ferroelectric Halide Perovskites. *Proc. Natl. Acad. Sci. U. S. A.* **2014**, *111*, 6900–6904.
47. Brivio, F.; Butler, K. T.; Walsh, A.; van Schilfgaarde, M. Relativistic Quasiparticle Self-Consistent Electronic Structure of Hybrid Halide Perovskite Photovoltaic Absorbers. *Phys. Rev. B: Condens. Matter Mater. Phys.* **2014**, *89*, 155204.
48. Amat, A.; Mosconi, E.; Ronca, E.; Quarti, C.; Umari, P.; Nazeeruddin, M. K.; Grätzel, M.; De Angelis, F. Cation-Induced Band-Gap Tuning in Organohalide Perovskites: Interplay of Spin-Orbit Coupling and Octahedra Tilting. *Nano Lett.* **2014**, *14*, 3608–3616.
49. Stroppa, A.; Di Sante, D.; Barone, P.; Bokdam, M.; Kresse, G.; Franchini, C.; Whangbo, M.-H.; Picozzi, S. Tunable Ferroelectric Polarization and its Interplay with Spin-Orbit Coupling in Tin Iodide Perovskites. *Nat. Commun.* **2014**, *5*, 5900.
50. Kutes, Y.; Ye, L.; Zhou, Y.; Pang, S.; Huey, B. D.; Padture, N. P. Direct Observation of Ferroelectric Domains in Solution-Processed $CH_3NH_3PbI_3$ Perovskite Thin Films. *J. Phys. Chem. Lett.* **2014**, *5*, 3335–3339.
51. Giovanni, D.; Ma, H.; Chua, J.; Grätzel, M.; Ramesh, R.; Mhaisalkar, S.; Mathews, N.; Sum, T. C. Highly Spin-Polarized Carrier Dynamics and Ultralarge Photoinduced Magnetization in $CH_3NH_3PbI_3$ Perovskite Thin Films. *Nano Lett.* **2015**, *15*, 1553–1558.
52. Even, J. Pedestrian Guide to Symmetry Properties of the Reference Cubic Structure of 3D All-Inorganic and Hybrid Perovskites. *J. Phys. Chem. Lett.* **2015**, *6*, 2238–2242.
53. Vajna, S.; Simon, E.; Szilva, A.; Palotas, K.; Ujfalussy, B.; Szunyogh, L. Higher-Order Contributions to the Rashba-Bychkov Effect with Application to the Bi/Ag(111) Surface Alloy. *Phys. Rev. B: Condens. Matter Mater. Phys.* **2012**, *85*, 075404.
54. Poglitsch, A.; Weber, D. Dynamic Disorder in Methylammoniumtrihalogenoplumbates (II) Observed by Millimeter-Wave Spectroscopy. *J. Chem. Phys.* **1987**, *87*, 6373–6378.
55. Yamada, K.; Kuranaga, Y.; Ueda, K.; Goto, S.; Okuda, T.; Furukawa, Y. Phase Transition and Electric Conductivity of $ASnCl_3$ (A = Cs and CH_3NH_3). *Bull. Chem. Soc. Jpn.* **1998**, *71*, 127–134.
56. Yamada, K.; Mikawa, K.; Okuda, T.; Knight, K. S. Static and Dynamic Structures of $CD_3ND_3GeCl_3$ Studied by TOF High Resolution Neutron Powder Diffraction and Solid State NMR. *Dalton Trans.* **2002**, 2112–2118.
57. Chi, L.; Swainson, I.; Cranswick, L.; Her, J.-H.; Stephens, P.; Knop, O. The Ordered Phase of Methylammonium Lead Chloride $CH_3ND_3PbCl_3$. *J. Solid State Chem.* **2005**, *178*, 1376–1385.
58. Filip, M. R.; Eperon, G. E.; Snaith, H. J.; Giustino, F. Steric Engineering of Metal-Halide Perovskites with Tunable Optical Band Gaps. *Nat. Commun.* **2014**, *5*, 5757.
59. Katan, C.; Pedesseau, L.; Kepenekian, M.; Rolland, A.; Even, J. Interplay of Spin-Orbit Coupling and Lattice Distortion in Metal Substituted 3D Tri-Chloride Hybrid Perovskites. *J. Mater. Chem. A* **2015**, *3*, 9232–9240.
60. Stoumpos, C. C.; Frazer, L.; Clark, D. J.; Kim, Y. S.; Rhim, S. H.; Freeman, A. J.; Ketterson, J. B.; Jang, J. I.; Kanatzidis, M. G. Hybrid Germanium Iodide Perovskite Semiconductors: Active Lone Pairs, Structural Distortions, Direct and Indirect Energy Gaps, and Strong Nonlinear Optical Properties. *J. Am. Chem. Soc.* **2015**, *137*, 6804–6819.
61. Stoumpos, C. C.; Malliakas, C. D.; Kanatzidis, M. G. Semiconducting Tin and Lead Iodide Perovskites with Organic Cations: Phase Transitions, High Mobilities, and Near-Infrared Photoluminescent Properties. *Inorg. Chem.* **2013**, *52*, 9019–9038.
62. Knutson, J. L.; Martin, J. D.; Mitzi, D. B. Tuning the Band Gap in Hybrid Tin Iodide Perovskite Semiconductors Using Structural Templating. *Inorg. Chem.* **2005**, *44*, 4699–4705.
63. Braun, M.; Frey, W. Crystal Structure of Bis(benzylammonium) Lead Tetrachloride, $(C_7H_7NH_3)_2PbCl_4$. *Z. Kristallogr. New Cryst. Struct.* **1999**, *214*, 331–332.
64. Liao, W.-Q.; Zhang, Y.; Hu, C.-L.; Mao, J.-G.; Ye, H.-Y.; Li, P.-F.; Huang, S. D.; Xiong, R.-G. A Lead-Halide Perovskite

Molecular Ferroelectric Semiconductor. *Nat. Commun.* **2015**, *6*, 7338.
65. Baikie, T.; Fang, Y.; Kadro, J. M.; Schreyer, M.; Wei, F.; Mhaisalkar, S. G.; Grätzel, M.; White, T. J. Synthesis and Crystal Chemistry of the Hybrid Perovskite $(CH_3NH_3)PbI_3$ for Solid-State Sensitised Solar Cell Applications. *J. Mater. Chem. A* **2013**, *1*, 5628–5641.
66. Petersen, L.; HedegÅrd, A. Simple Tight-Binding Model of Spin-Orbit Splitting of sp-Derived Surface States. *Surf. Sci.* **2000**, *459*, 49–56.
67. Kane, C. L.; Mele, E. J. Quantum Spin Hall Effect in Graphene. *Phys. Rev. Lett.* **2005**, *95*, 226801.
68. Konschuh, S.; Gmitra, M.; Fabian, J. Tight-Binding Theory of the Spin-Orbit Coupling in Graphene. *Phys. Rev. B: Condens. Matter Mater. Phys.* **2010**, *82*, 245412.
69. Ast, C. R.; Gierz, I. sp-Band Tight-Binding Model for the Bychkov-Rashba Effect in a Two-Dimensional Electron System Including Nearest-Neighbor Contributions from an Electric Field. *Phys. Rev. B: Condens. Matter Mater. Phys.* **2012**, *86*, 085105.
70. Swainson, I. P.; Hammond, R. P.; Soullière, C.; Knop, O.; Massa, W. Phase Transitions in the Perovskite Methylammonium Lead Bromide, $CH_3ND_3PbBr_3$. *J. Solid State Chem.* **2003**, *176*, 97–104.
71. Umari, P.; Mosconi, E.; De Angelis, F. Relativistic GW Calculations on $CH_3NH_3PbI_3$ and $CH_3NH_3SnI_3$ Perovskites for Solar Cell Applications. *Sci. Rep.* **2014**, *4*, 4467.
72. Datta, S.; Das, B. Electronic Analog of the Electrooptic Modulator. *Appl. Phys. Lett.* **1990**, *56*, 665–667.
73. Yin, C.; Yuan, H.; Wang, X.; Liu, S.; Zhang, S.; Tang, N.; Xu, F.; Chen, Z.; Shimotani, H.; Iwasa, Y.; et al. Tunable Surface Electron Spin Splitting with Electric Double-Layer Transistors Based on InN. *Nano Lett.* **2013**, *13*, 2024–2029.
74. Kim, K.-H.; Um, D.-S.; Lee, H.; Lim, S.; Chang, J.; Koo, H. C.; Oh, M.-W.; Ko, H.; Kim, H. Gate-Controlled Spin-Orbit Interaction in InAs High-Electron Mobility Transistor Layers Epitaxially Transferred onto Si Substrates. *ACS Nano* **2013**, *7*, 9106–9114.
75. Di Sante, D.; Barone, P.; Bertacco, R.; Picozzi, S. Electric Control of the Giant Rashba Effect in Bulk GeTe. *Adv. Mater.* **2013**, *25*, 509–513.
76. Liu, Q.; Guo, Y.; Freeman, A. J. Tunable Rashba Effect in Two-Dimensional LaOBiS2 Films: Ultrathin Candidates for Spin Field Effect Transistors. *Nano Lett.* **2013**, *13*, 5264–5270.
77. Citro, R.; Romeo, F.; Marinaro, M. Zero-Conductance Resonances and Spin Filtering Effects in Ring Conductors Subject to Rashba Coupling. *Phys. Rev. B: Condens. Matter Mater. Phys.* **2006**, *74*, 115329.
78. Aharony, A.; Tokura, Y.; Cohen, G. Z.; Entin-Wohlman, O.; Katsumoto, S. Filtering and Analyzing Mobile Qubit Information via Rashba-Dresselhaus-Aharonov-Bohm Interferometers. *Phys. Rev. B: Condens. Matter Mater. Phys.* **2011**, *84*, 035323.
79. Matityahu, S.; Aharony, A.; Entin-Wohlman, O.; Tarucha, S. Spin Filtering in a Rashba-Dresselhaus-Aharonov-Bohm Double-Dot Interferometer. *New J. Phys.* **2013**, *15*, 125017.
80. Winkler, R. Spin Polarization of Quasi-Two-Dimensional Hole Systems. *Phys. Rev. B: Condens. Matter Mater. Phys.* **2005**, *71*, 113307.
81. Winkler, R. Spin Orientation and Spin Precession in Inversion-Asymmetric Quasi-Two-Dimensional Electron Systems. *Phys. Rev. B: Condens. Matter Mater. Phys.* **2004**, *69*, 045317.
82. Winkler, R. Spin Density Matrix of Spin-3/2 Hole Systems. *Phys. Rev. B: Condens. Matter Mater. Phys.* **2004**, *70*, 125301.
83. Liu, Q.; Zhang, X.; Jin, H.; Lam, K.; Im, J.; Freeman, A. J.; Zunger, A. Search and Design of Nonmagnetic Centrosymmetric Layered Crystals with Large Local Spin Polarization. *Phys. Rev. B: Condens. Matter Mater. Phys.* **2015**, *91*, 235204.
84. Soler, J. M.; Artacho, E.; Gale, J. D.; García, A.; Junquera, J.; Ordejón, P.; Sánchez-Portal, D. The SIESTA Method for *Ab Initio* Order-N Materials Simulation. *J. Phys.: Condens. Matter* **2002**, *14*, 2745–2779.
85. Artacho, E.; Anglada, E.; Diéguez, O.; Gale, J. D.; García, A.; Junquera, J.; Martin, R. M.; Ordejón, P.; Pruneda, J. M.; Sánchez-Portal, D.; et al. The SIESTA method; Developments and Applicability. *J. Phys.: Condens. Matter* **2008**, *20*, 064208.
86. Perdew, J. P.; Burke, K.; Ernzerhof, M. Generalized Gradient Approximation Made Simple. *Phys. Rev. Lett.* **1996**, *77*, 3865–3868.
87. Troullier, N.; Martins, J. L. Efficient Pseudopotentials for Plane-Wave Calculations. *Phys. Rev. B: Condens. Matter Mater. Phys.* **1991**, *43*, 1993–2006.
88. Artacho, E.; Sánchez-Portal, D.; Ordejón, P.; García, A.; Soler, J. M. Linear-Scaling *Ab-Initio* Calculations for Large and Complex Systems. *Phys. Status Solidi B* **1999**, *215*, 809–817.
89. Fernández-Seivane, L.; Oliveira, M. A.; Sanvito, S.; Ferrer, J. On-site Approximation for Spin-Orbit Coupling in Linear Combination of Atomic Orbitals Density Functional Methods. *J. Phys.: Condens. Matter* **2006**, *18*, 7999–8013.
90. Kresse, G.; Furthmüller, J. Efficiency of *Ab-Initio* Total Energy Calculations for Metals and Semiconductors Using a Plane-Wave Basis Set. *Comput. Mater. Sci.* **1996**, *6*, 15–50.
91. Kresse, G.; Furthmüller, J. Efficient Iterative Schemes for *Ab-Initio* Total-Energy Calculations Using a Plane-Wave Basis Set. *Phys. Rev. B: Condens. Matter Mater. Phys.* **1996**, *54*, 11169–11186.